Wafer-Scale Hybrid Integration of InP DFB Lasers on Si Photonics by Flip-Chip Bonding With sub-300 nm Alignment Precision

Aleksandrs Marinins [ID], Sebastian Hänsch, Huseyin Sar, François Chancerel [ID], Negin Golshani, Hsiao-Lun Wang, Artemisia Tsiara [ID], David Coenen [ID], *Student Member, IEEE*, Peter Verheyen [ID], Giovanni Capuz [ID], Yannick De Koninck, Ozan Yilmaz, Geert Morthier [ID], Filip Schleicher [ID], Geraldine Jamieson, Stuart Smyth, Andrew McKee, Yoojin Ban, Marianna Pantouvaki [ID], *Member, IEEE*, Douglas Charles La Tulipe, and Joris Van Campenhout [ID], *Member, IEEE*

Abstract—InP DFB lasers are flip-chip bonded to 300 mm Si photonic wafers using a pick-and-place tool with an advanced vision system, realizing high-precision and high-throughput passive assembly. By careful co-design of the InP-Si Photonics electrical, optical and mechanical interface, as well as dedicated alignment fiducials, sub-300 nm post-bonding alignment precision is realized in a 25 s cycle time. Optical coupling losses of -1.5 ± -0.5 dB are achieved at 1550 nm wavelength after epoxy underfill, with up to 40 mW of optical power coupled to the SiN waveguides on the Si photonics wafer. The bonding interface adds less than 10% to the series resistance of the laser diodes and post-bonding thermal resistance is measured to be 76 K/W (or 27 K.mm/W), mostly dominated by heat spreading resistance in the InP lasers as suggested by in-depth thermal modeling. Although the assembled lasers suffer from significant, unintentional optical backreflection from the fiber grating couplers used for optical characterization, laser linewidths well below 1 MHz have been measured under specific drive conditions, as supported by a detailed laser noise analysis. Finally, we demonstrate the ability of bonded laser assemblies to pass early reliability tests.

Index Terms—Flip-chip devices, hybrid integrated circuits, semiconductor lasers, silicon photonics.

Aleksandrs Marinins, Huseyin Sar, François Chancerel, Negin Golshani, Hsiao-Lun Wang, Artemisia Tsiara, David Coenen, Peter Verheyen, Giovanni Capuz, Filip Schleicher, Geraldine Jamieson, Yoojin Ban, and Joris Van Campenhout are with the IMEC, 3001 Leuven, Belgium (e-mail: aleksandrs.marinins@imec.be; huseyin.sar@imec.be; francois.chancerel@imec.be; negin.golshani@imec.be; hsiao-lun.wang@imec.be; artemisia.tsiara@imec.be; david.coenen@imec.be; peter.verheyen@imec.be; giovanni.capuz@imec.be; filip.schleicher@imec.be; geraldine.jamieson@imec.be; yoojin.ban@imec.be; joris.vancampenhout@imec.be).

Sebastian Hänsch is with the ASMPT Amicra, 93055 Regensburg, Germany (e-mail: sebastian.haensch@asmpt.com).

Yannick De Koninck was with the IMEC, 3001 Leuven, Belgium. He is now with the NVIDIA Corporation, 4000 Roskilde, Denmark (e-mail: ydekoninck@nvidia.com).

Ozan Yilmaz was with the IMEC, 3001 Leuven, Belgium. He is now with the Aeva Technologies, Mountain View, CA 94043 USA (e-mail: oyilmaz@aeva.ai).

Geert Morthier is with the Ghent University, Department of Information Technology, Ghent University, 9052 Gent, Belgium (e-mail: geert.morthier@ugent.be).

Stuart Smyth and Andrew McKee are with the Sivers Photonics, Glasgow G72 0BN, U.K. (e-mail: stuart.smyth@sivers-photonics.com; andrew.mckee@sivers-photonics.com).

Marianna Pantouvaki was with the IMEC, 3001 Leuven, Belgium. She is now with the Microsoft Corporation, Cambridge CB1 2FB, U.K. (e-mail: pantouvakim@gmail.com).

Douglas Charles La Tulipe was with the IMEC, 3001 Leuven, Belgium. He is now with the Draper Laboratory, Cambridge, MA 02139 USA (e-mail: dlip410@gmail.com).

Color versions of one or more figures in this article are available at https://doi.org/10.1109/JSTQE.2022.3223641.

Digital Object Identifier 10.1109/JSTQE.2022.3223641

I. INTRODUCTION

S i PHOTONICS (SiPho) transceivers are being deployed at an accelerating pace to keep up with increasing demands for communication in data centers and high-performance computing systems. Future applications will require advanced multiwavelength light sources, integrated into Si photonic chips [1], [2]. Integrated light sources are also a key component of LiDAR and other sensors based on SiPho technology [3]. Today, various laser integration approaches are considered, ranging from laser micro-packages, flip-chip bonding [4], micro-transfer printing [5], die-to-wafer bonding [6] and direct III-V epitaxial growth on the Si substrate [7]. Each method has its own benefits and challenges and different cost structure.

In this work, we focus on hybrid laser integration, where prefabricated and tested III-V laser light sources are flip-chip bonded to 300 mm SiPho wafers, as illustrated in Fig. 1. A key benefit of this approach is the relatively low development costs, as well as the simplicity and flexibility of its supply chain. This integration approach is particularly well suited for applications requiring a relatively low number of light sources per SiPho unit area. Applications requiring a larger number of light sources may benefit from higher throughput integration approaches, at the expense of higher upfront development costs.

One of the key challenges of flip-chip integration is the placement precision, which directly affects the laser-SiPho optical coupling loss. This is particularly important for lasers with small mode field diameters, where coupling efficiency is highly sensitive to misalignment. In this work, we leverage an advanced vision-driven dynamic alignment pick-and-place tool (ASM Amicra Nano System), featuring high post-bonding alignment precision, to address this challenge at wafer scale with
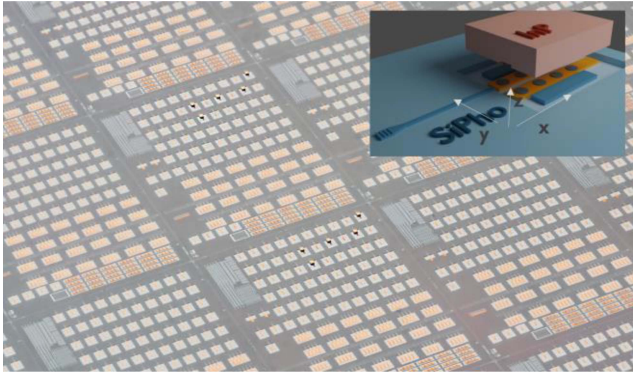
Fig. 1. Camera image of a 300 mm SiPho wafer with wafer-scale flip-chip bonded InP laser diodes. The inset shows a 3D schematic of the flip-chip laser bonding test site.

a relatively high throughput of >100 (laser) units per hour. The opto-mechanical interface between the SiPho wafer and the InP DFB lasers was carefully co-designed and implemented in a commercially available InP laser technology (Sivers Photonics, Fig. 2(a)).

II. LASER FLIP-CHIP INTEGRATION

A. Interface Design and Simulations

First, we define the specifications for the assembly process to achieve a coupling efficiency of lower than 2 dB, supported by detailed optical simulations of the laser-SiPho interface, using Lumerical 3D FDTD software. The coupling interface and test site are schematically shown in the inset of Figs. 1 and 2(b). Light with 1550 nm wavelength from the InP DFB laser is butt coupled to a 400 nm thick PECVD SiN waveguide (Fig. 2(c)), implemented on the SiPho wafer, having a 2225 nm-thick bottom oxide layer, and a 2165 nm-thick top oxide. The 840 nm wide SiN waveguide is tapered down in the laser coupling interface to better match the laser mode. In this work, we only explored a simple, straight inversely tapered waveguide edge coupler design. More advanced couplers with lower insertion loss [8] and higher misalignment tolerance [9] will be explored in future work. First, the optimal SiN taper tip width is identified, based on the maximum field overlap between the InP laser mode and the SiN mode (Fig 2(d)–(f)), assuming perfect alignment. The laser mode is approximately 2 µm wide and 1 µm high, reflecting the tight mode confinement in the InP waveguide, and necessitating the need for a pick-and-place process with sub-micron precision. The mode slightly expands while propagating in the 500 nm-wide gap between the InP laser and the SiPho facets. As can be seen in Fig 3(a), the best coupling efficiency is achieved for a SiN taper tip width of 350 nm, yielding -1.6 dB coupling loss assuming air between the InP and the SiPho facets. Filling this gap with an index-matching epoxy reduces coupling loss to -1.1 dB. The 0.5 dB improvement can be partially explained by a reduced reflection at the SiPho facet. As there is no anti-reflection coating on this SiN/oxide facet, the index contrast reaches $\sim$30% with an air gap. The epoxy has a refractive index (RI) of 1.56 at 1550 nm wavelength, which is
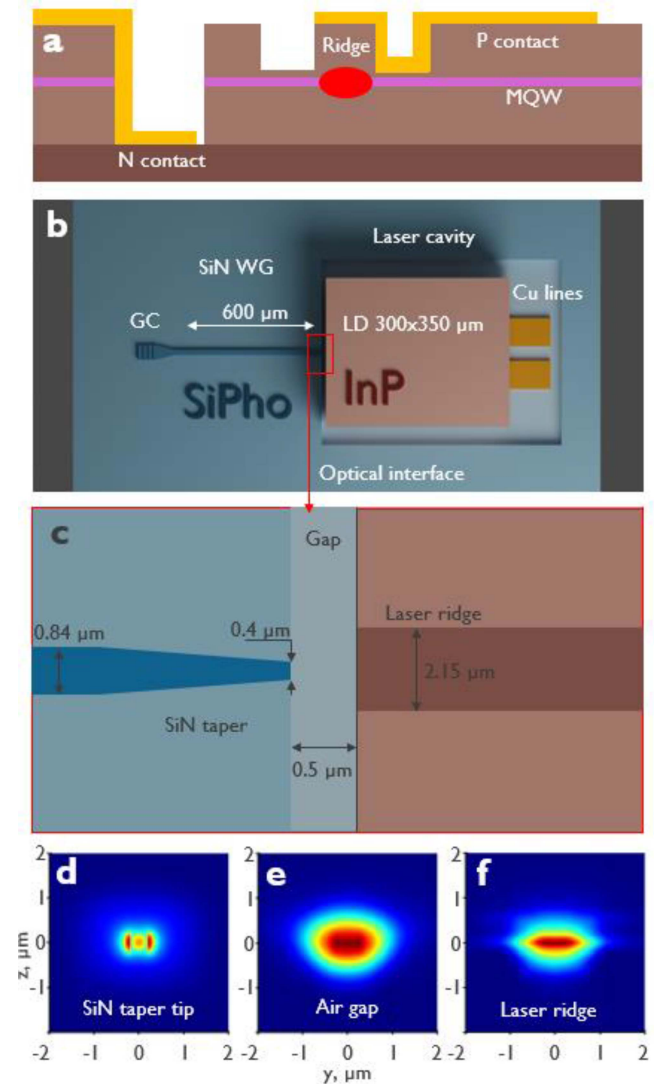

Fig. 2. Cross-section schematic of InP laser with both contacts on frontside (a). Top-view schematic of assembly test vehicle (b). Laser-SiPho optical interface schematic (not to scale) (c). Mode profiles of light propagating from laser (d) to SiPho facet (e) through air gap (f).

better matched with the SiN taper tip effective index (n $\sim$1.6), minimizing Fresnel reflections at this interface.

Next, the sensitivity to alignment errors was modelled to set the specifications for the placement process (Fig. 3(b)–(c)). We explored 3 translational (x, y, z) and 3 rotational (pitch, yaw, roll) misalignments. As our mechanical interface includes pillars for passive vertical alignment, 2 translational and 1 rotational degrees of freedom remain. In Fig. 3(b)–(c), we show the simulated misalignment sensitivity for a 350 nm wide SiN taper, which yields the lowest insertion loss. Since the laser mode is narrower in the vertical direction, the coupling efficiency is sensitive mostly to vertical misalignment (Fig. 3(b)). After evaluation of excess loss from translational misalignment, we defined the placement precision specs as <500 nm (mean$+3\sigma$) for x alignment, <300 nm for y alignment, and <200 nm for z alignment.
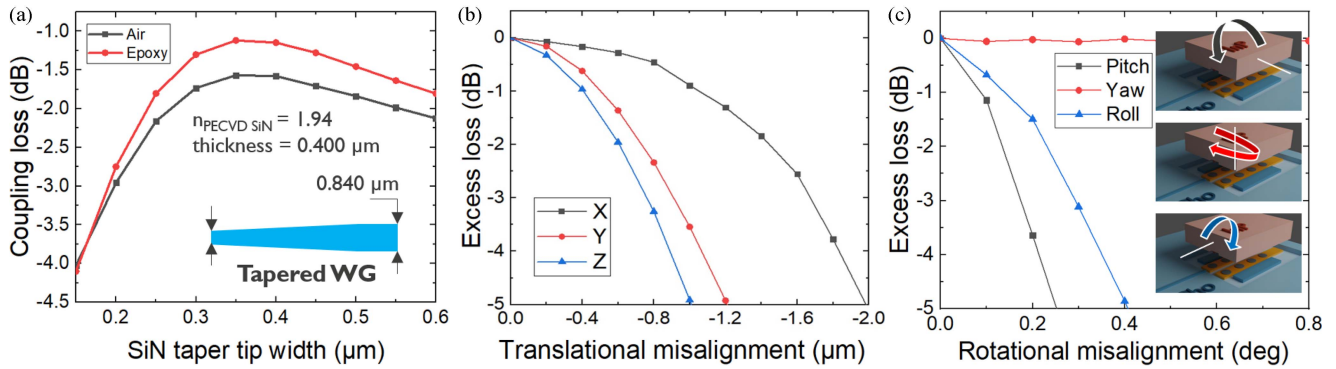
Fig. 3. Coupling loss vs. SiN taper tip width for air and epoxy between DFB laser facet and SiPho facet (a). Simulated translational (b) and rotational (c) alignment sensitivity for 350 nm wide SiN taper tip. Inset schematically shows rotational degrees of freedom.
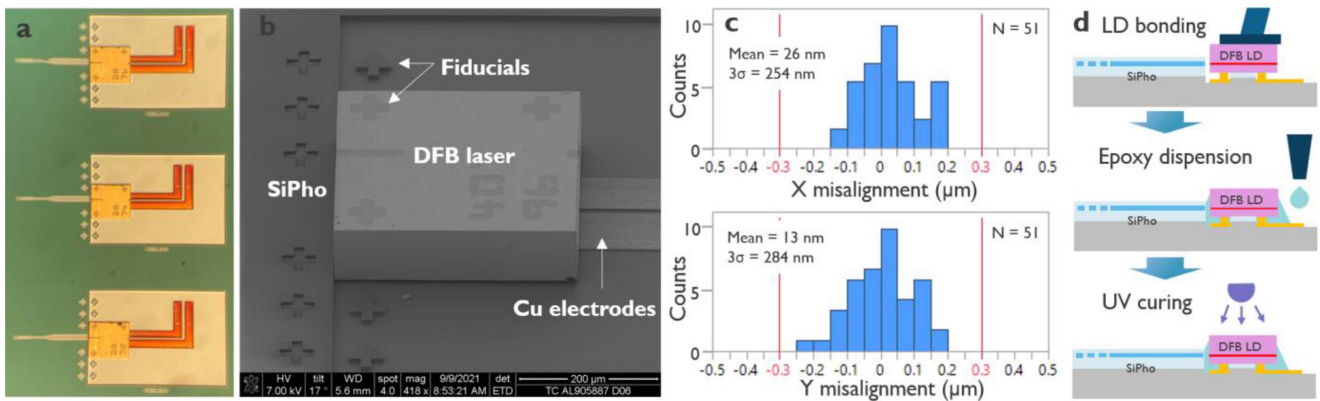

Fig. 4. Optical microscope image of an array of bonded LDs (a). A tilted SEM image of the LD-SiPho assembly before underfill (b). Histograms showing LD xy placement statistics (b). Schematic of an assembly flow in (d).

Looking at rotational sensitivity, a yaw misalignment (rotation around z axis) creates a negligible excess loss when below 1 degree (Fig. 3(c)). Based on geometry, yaw misalignment will be limited to 0.2 degree for a 0.5 µm laser-SiPho facet distance. On the other hand, an analysis of pitch and roll misalignment demonstrates significant excess loss in case of failure to properly land the LD on the vertical alignment pedestals. The pitch should be <0.05 degree and roll should be <0.09 degree to stay within a reasonable excess loss of ∼0.5 dB. From a practical point of view, this means that the pedestals and corresponding laser surfaces should be well matched in dimensions and free of particles, and that the wafer chuck and bonding head in the flip-chip tool needs to be accurately leveled.

B. Assembly Process Development

InP DFB laser diodes (LD) were co-designed with the SiPho interface and manufactured by Sivers Photonics on the InP100 platform. The laser diodes operate in the C-band and have both electrodes on the frontside as well as mechanical alignment features, facilitating the p-side down flip-chip bonding process. The nominal dimensions of the laser dies are 300 µm (W) x 350 µm (L) x 100 µm (H). The receiving 300 mm SiPho wafer contains laser bonding sites with dry-etched cavities to host the

InP LDs, featuring co-designed vertical alignment pillars, Cu redistribution lines, and Cu/Ni/Sn bumps plated with a standard CMOS process to electrically connect to the Au electrodes of the LDs. Both the LD dies and the SiPho wafer contain matching cross-shaped fiducials, which are used by the assembly tool imaging system for realizing high-precision LD placement along the x-y axes (Fig. 4(a), (b)). For vertical alignment (z axis), which has the tightest alignment spec, passive alignment is exploited by placing the LD on limiting pedestals made in the SiPho wafer. These pedestals are defined by highly selective etch processes, with better than 10 nm relative precision along the z axis between the pedestal top surface and the SiN waveguide bottom surface. Similarly, complementary trenches are precisely defined on the LD front surface to match the SiPho pedestals.

First, the imaging system in the assembly tool aligns a LD in the xy plane, and subsequently, the bondhead presses the LD against the Cu/Ni/Sn bumps and vertical alignment pedestals. The SiPho wafer is then locally heated with a laser from the backside, to reflow the Sn and electrically connect with the Au contacts on the LD. During the Sn reflow process, the LD lands on the SiPho vertical alignment pedestals. Several process parameters, such as bond force, bond pressure position, Sn reflow temperature and time, were optimized to achieve the best bonding results. After these process optimizations, we have achieved
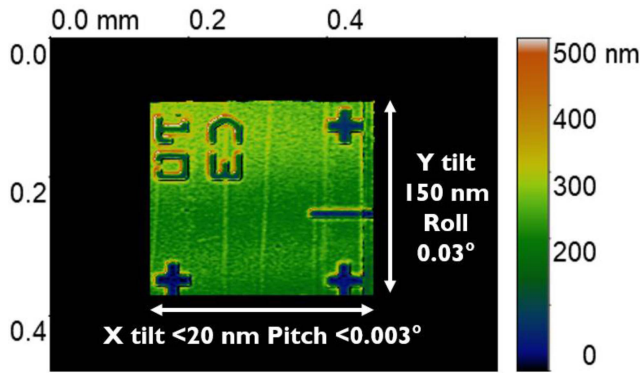
Fig. 5.   Bonded LD profile measurement with white-light interferometry.

a post-bonding x and y placement accuracy (3σ) of 254 nm and 284 nm, respectively, centered at the mean values of 26 nm and 13 nm, as illustrated in Fig. 4(c). This data was collected from 51 LDs bonded on a target wafer within one run. The measurement precision of the camera system is ∼50 nm. Vertical alignment accuracy can be evaluated by doing a cross-section of assembly and inspecting mechanical interface in a scanning electron microscope (SEM). However, this method is destructive and has low throughput. Therefore, we adopted an indirect measurement method utilizing a white-light interferometer. This technique allows to measure the tilt of a bonded LD, which indicates how well the die landed on vertical alignment pedestals. A typical example (Fig. 5) shows a bonded LD die with <20 nm and ∼150 nm height variation across the x and y axes respectively, which corresponds to <0.003 degree pitch and 0.03 degree roll. This is well within the angular misalignment specification. The bonding cycle time is approximately 25 seconds.

After the reflow bonding of the lasers, an epoxy underfill is applied (Fig. 4(d)), which is required to address several critical points:
- improved bonding strength and mechanical stability
- reduction of back-reflections from SiPho interface
- passivation of electrical contacts,
- improved heat dissipation.

A commercially available optical UV-curable epoxy was applied by the dispensing unit within the ASM Amicra Nano System and then UV cured. In this way, all LD packaging steps are implemented within a single assembly platform.

III. MEASUREMENT RESULTS

A. Optical Coupling Efficiency

We recorded post-assembly L-I-V curves and laser emission spectra to evaluate the bonding process. As seen in Fig. 2(b), the test circuit consists of a bonded LD, a single-mode tapered SiN waveguide and a SiN fiber grating coupler on the 300 mm SiPho wafer. The LD-SiPho coupling loss is derived by comparing the measured fiber-coupled LD optical power of the assembly with the output power of the same LD before bonding, while calibrating out the insertion loss of the grating coupler (measured separately on a reference structure on the same reticle). The

overall measurement error of the extracted coupling loss is conservatively estimated to be ±0.5 dB.

Fig. 6(a) shows the obtained coupling loss values for different SiN taper tip widths, before and after epoxy underfill application. Before epoxy encapsulation, the coupling loss values are in the range −2.5±1 dB. After the underfill process, the coupling losses are improved to −1.5±0.5 dB, particularly for 350 nm and 400 nm wide SiN tapers. As discussed in Section II.A, an improvement of about 0.5 dB can be expected based on the optical simulations. Further improvement may come from lowered scattering losses at the sidewall roughness of the SiPho facet after application of the index-matching epoxy.

The coupling loss values measured after applying the underfill are close to the simulated coupling loss with epoxy in the LD-SiPho gap (−1.1 dB, see Fig. 3(a)). In addition to improving coupling loss, the underfill process also improves the mechanical reliability of the assemblies: shear tests results are discussed in paragraph D.

Coupling losses of −1.5 dB are on-par with some of the best reported flip-chip processes using active alignment [4]. In our work, we obtain competitive coupling efficiencies without requiring integrated mode size expanders in the InP LDs, making the assembly process more generally applicable. In addition, leveraging a pure vision based passive alignment, the assembly process is simplified and can be done in a relatively short cycle time of 25 s.

Fig 6(b)–(c) show the post-bond, SiN waveguide-referred L-I curves of several assemblies, overlaid on the LD L-I curves before bonding. Most of the variation in coupled optical power originates from the LDs in this batch, which had variation in emitted power due to an underlying design split. Up to 40 mW of optical power is coupled into the SiN waveguide at a drive current of 200 mA. The ripples in the L-I curves are a consequence of the relatively strong optical feedback from the SiN grating coupler back into the DFB laser cavity. The cavity length corresponding to a 2π phase shift induced by one L-I curve ripple period (25–30 mA) is matching with SiN waveguide length with a grating coupler. SiPho facet distance to laser diode is below 1 μm, therefore, it is too short to create L-I curve ripples with observed period. A backreflection strength of 4% (−14 dB) is estimated from the Fabry-Perot ripple amplitude in the measured transmission spectrum of a short SiN reference waveguide with two SiN grating couplers. This is a known design issue, which can be fixed in a future design by implementing a grating coupler with low backreflection [10]. Paragraph C includes a deeper study of these feedback effects on the laser emission properties.

The electrical characteristics of the laser assemblies were evaluated by comparing V-I curves before and after bonding with epoxy underfill (Fig. 7). The extracted series resistances are 15.40±0.15 Ohm and 16.55±0.07 Ohm (sans outlier) for LDs before and after assembly, respectively. Only ∼1.1 Ohm is added after the assembly process, which suggests a robust electrical interface with SiPho metallization.

To verify the repeatability of the packaged LD measurements, we repeatedly recorded L-I-V curves in 15 drive current ramp cycles from 0 to 200 mA, at room temperature. Both V-I and L-I curves are very reproducible, including the L-I ripples.
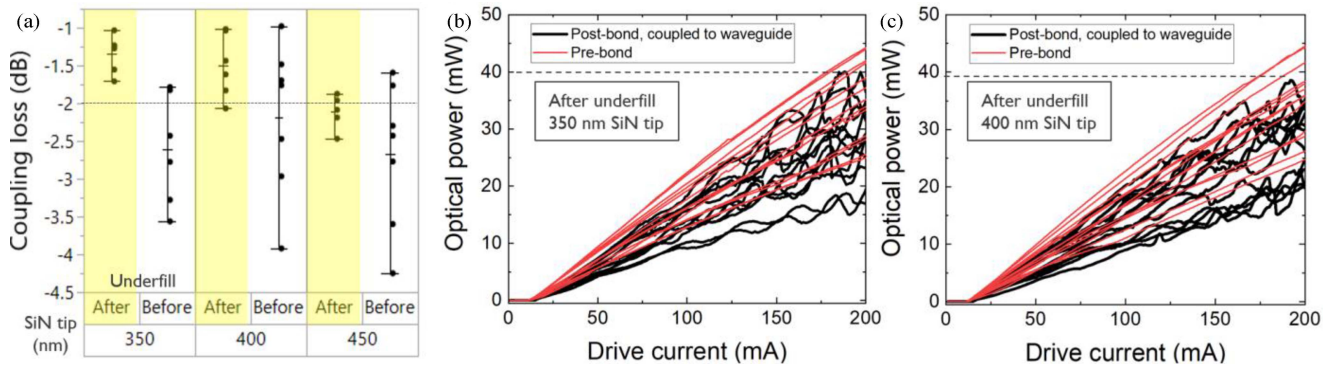
Fig. 6. Optical coupling loss before and after epoxy underfill for 3 different SiN taper tip widths (a). Optical power coupled to SiN waveguides versus drive current for 350 nm (b) and 400 nm (c) SiN taper tip width (after epoxy underfill). Pre-bond L-I curves are added for reference.
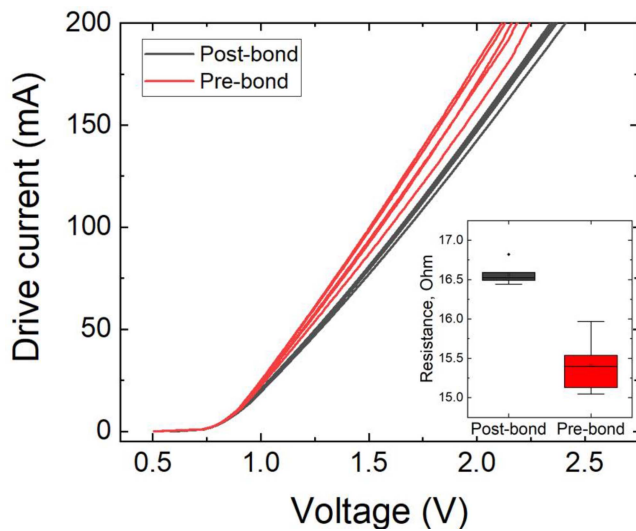

Fig. 7. V-I characteristics of LDs before and after assembly. Inset shows a series resistance change.

Fig. 8. Packaged laser L-I curves at different chuck temperatures in logarithmic (a) and linear (b) scale.

We also evaluated the performance of bonded lasers at different SiPho wafer temperatures. This test was carried out using an earlier set of bonded lasers with higher coupling loss and up to ~20 mW waveguide-coupled optical power at room temperature. The wafer chuck temperature was varied from 25 °C to 65 °C and L-I curves were recorded (example shown in Fig. 8). Although the varying ripples in the L-I curves complicate an accurate comparison of threshold current and slope efficiency, up to 16 mW of optical power is coupled at 65 °C, a reduction of ~30% compared to 25 °C. The repeated measurement at 25 °C (black line) overlaps with the initial measurement (blue line), which shows that the laser assembly is stable after such operation temperature ramping. In the next paragraph, the thermal properties of the laser assembly are derived from experimental data and compared with thermal modeling results.

B. Thermal Performance and Modeling

For reliable operation, it is imperative that the laser temperature is kept as low as possible. Furthermore, laser performance degrades at elevated temperatures: lasing efficiency drops and
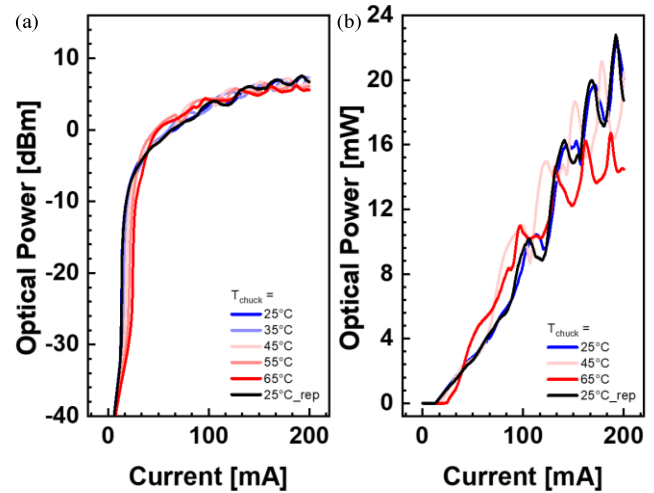
threshold current increases [11]. In this section, the thermal resistance of the bonded laser is determined experimentally, and this result is compared with a finite-element thermal model. The model allows to determine the laser operating temperature, for the case with and without epoxy underfill.

The laser thermal resistance is determined by the following equation [12], [13]:

$$R_{th} = \left(\frac{\partial \lambda}{\partial T}\right)^{-1} \left(\frac{\partial \lambda}{\partial P}\right), \qquad (1)$$

where λ is the laser wavelength, T is the laser temperature and P is the thermally dissipated power. The laser wavelength slopes are measured experimentally by increasing the wafer chuck temperature and increasing the laser drive current (Fig. 9). Following this method, a laser thermal resistance of 75.9 ± 16.3 K/W is extracted. For comparison with laser integration in other works, typically the performance is reported as the product (thermal resistance) x (length) [14]. The laser used in this work has a length of 350 μm, which results in a normalized laser thermal resistance of 26.6 K.mm/W. This value is competitive with recently demonstrated laser integration reported in literature:
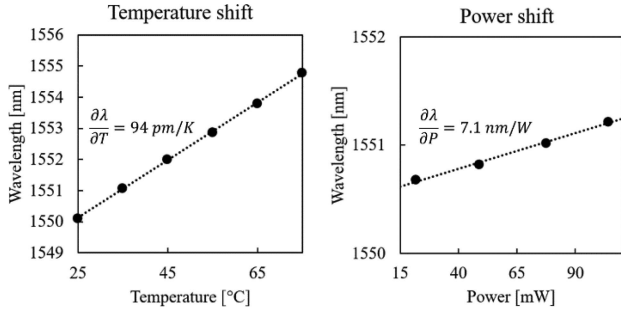
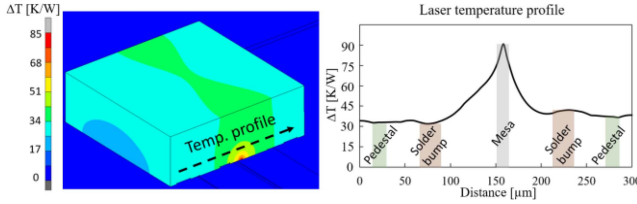Fig. 9.   Wavelength shift vs. temperature (left) and vs. power (right).

Fig. 10.   Finite element model of the bonded laser.

Fig. 11.   Laser temperature increase (left) and underfill impact on thermal resistance (right).

B. Song et al.[14] reported a normalized thermal resistance of 36.6 K.mm/W for a flip-chip integrated laser. For a micro-transfer printed laser, R. Loi et al. [15] reported a value between 19-46 K.mm/W. Finally, for heterogeneous laser integration, D. Shin et al. [16] reported a value between 20–34 K.mm/W.

Next, a finite-element thermal model of the laser is developed using the software Msc.Marc [17]. The computational domain is set as a 6×6 mm^2 containing the Si photonic carrier die, with the laser flip-chipped on top (Fig. 10). The simulated thermal resistance is 85.7 K/W, which matches reasonably well with the experimentally obtained value. The thermal resistance of the bonded laser is extracted in the model as the average laser mesa temperature per unit of dissipated thermal power. The model assumes that all heat generation occurs in the laser mesa, and no parasitic losses in the electrical contacts of the laser are considered. The total thermal resistance can be attributed to two main resistances along the heat transfer path from heat source (laser mesa) to heat sink (carrier die bottom face). Firstly, $\sim$50% of the total resistance comes from heat conduction in the InP of the laser itself. The other half comes from the thermal contact between the laser and the carrier die and the heat conduction through said carrier die. Furthermore, there is a secondary heat transfer path from the laser outer surfaces directly to the ambient air through natural convection. However, because the small surface area of the laser, this contribution to the total heat transfer is negligible ($<$0.04%). More details about the finite element modeling can be found in [18].

The laser temperature is now calculated in function of input current. The laser temperature increase is found by $\Delta T = R_{th} \cdot P_{th}$. The thermal power P_{th} is calculated by:

$$P_{th} = V \cdot I \cdot (1 - WPE\,(I,T)) \qquad (2)$$

where V is the voltage, I is the current and $WPE = P_{opt}/P_{el}$. Because of the temperature dependence of the wall plug efficien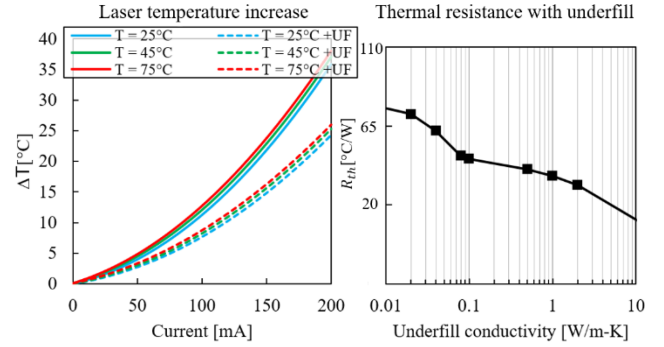cy, the temperature increase ΔT depends on the laser temperature. This results in an implicit equation for temperature increase that is solved iteratively. The wall plug efficiency is calculated from the measured L-I curves and the voltage is extracted from the measured laser I-V curves. The resulting laser characteristic temperature increase versus current shows that due to optical efficiency loss at higher temperatures, the self-heating is more severe at $T = 75$ °C compared to $T = 25$ °C (Fig. 11). Furthermore, the addition of epoxy underfill in the finite element model shows a decrease in thermal resistance of the bonded laser up to -31%, depending on the thermal conductivity of the epoxy. The epoxy underfill improves the thermal contact between the laser and carrier: it provides an alternative heat flow path from the laser mesa directly into the Si substrate below, partially mitigating the thermal spreading resistance in the laser itself.

We have also analyzed how much LD thermal expansion affects the mechanical alignment with SiPho. For the case when LD temperature is 100 °C, InP die of given dimensions expands by $\sim$129 nm laterally and $\sim$37 nm vertically. Such dimension change yields negligible misalignment loss below 0.1 dB (Fig. 3(b)).

C. Laser Linewidth and Frequency Noise

Laser frequency noise and spectral linewidth are fundamentally related, and they are critical to achieve high-performance semiconductor lasers. Many photonics applications require low noise and narrow linewidth lasers to offer better functionality. For example, coherent communication and FMCW Lidar require light sources with ultra-low frequency noise [19], [20]. Theoretical solitary laser linewidth can be fully expressed with spontaneous emission rate, laser output power and linewidth enhancement factor proposed by C. Henry [21]. For lasers coupled to silicon or silicon nitride waveguides, the frequency noise and linewidth can be affected by reflections in these passive waveguides as well, e.g., at the grating coupler [22]. The laser then becomes an external cavity laser and exhibits much more dispersion, which can affect the linewidth positively or negatively and to a lesser or greater extent depends on the amplitude and phase of the external reflection [23], [24], [25], [26]. In this section, frequency noise (FN) and linewidth measurement results of the bonded lasers are reported and discussed.
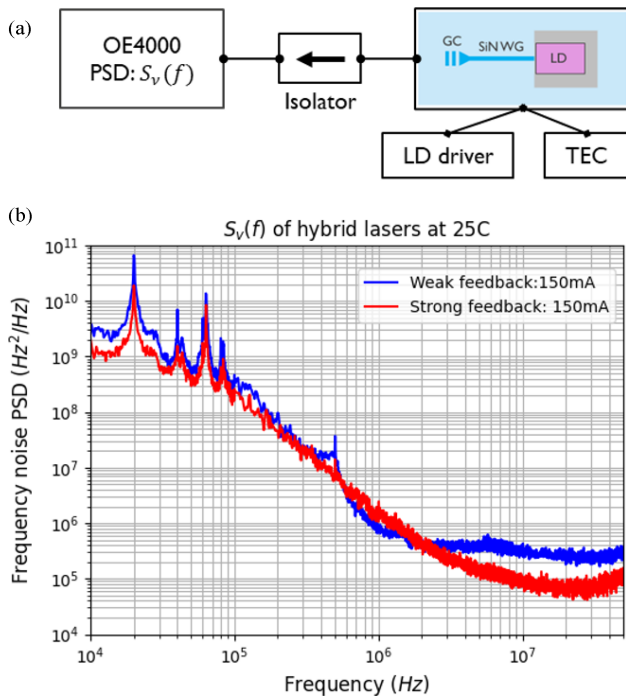
Fig. 12. Experimental setup for laser frequency noise characterization (a). Example of measured frequency noise power spectrum density from hybrid lasers with weak feedback (blue) and strong feedback (red). The Lorentzian linewidth of each trace is proportional to the white noise level of PSD, Sv^0 (b).

The effects of external feedback strength on laser linewidth are analyzed.

The Lorentzian linewidth, $\Delta\nu$, is directly obtained from the frequency noise power spectral density (PSD) $S_\nu(f)$, measured using the frequency/phase noise analyzer from OEwaves, Inc. Fig. 12(a) shows the schematic of the experimental setup. The laser chip temperature is controlled and driving current is supplied through DC probes. The light output from the grating coupler is first coupled to a cleaved single-mode fiber with fixed tilting angle and then connected to an optical isolator to prevent extra back-reflections from the rest of the optical path. Lastly the optical signal is fed into the OE4000 to measure $S_\nu(f)$. The Lorentzian linewidth is derived using the following equation [24]:

$$\Delta\nu_{Lorentzian} = \pi \times S_\nu^0 \qquad (3)$$

with S_ν^0 the spectral density of the white noise part from the FN PSD. Note that the system includes noises from both thermoelectric cooling (TEC) and the laser diode (LD) driver. Therefore, the same equipment is used during every measurement so the lasers' frequency noise can be compared fairly.

The linewidth $\Delta\nu$ under feedback can be qualitatively described using following equation [25], [26]:

$$\Delta\nu = \frac{\Delta\nu_0}{[1 + C \cdot \cos(\phi_{ext} + \tan^{-1}\alpha)]^2} , \qquad (4)$$

where $\Delta\nu_0$ is the solitary laser linewidth, C is the effective feedback strength coefficient, ϕ_{ext} is the feedback phase and α is the laser linewidth enhancement factor. In our measurements, we
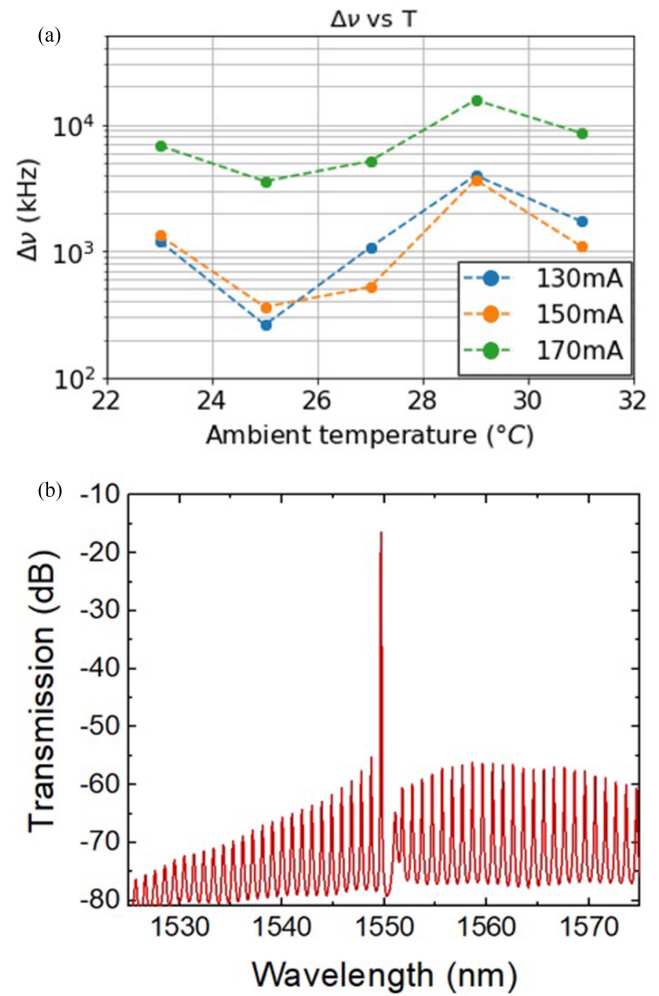

Fig. 13. Measured Lorentzian linewidth vs. ambient temperature for laser assembly at different drive currents (a) and a typical laser emission spectrum after packaging (b).

changed the feedback phase by varying the temperature, which mainly changes the emission wavelength of the DFB laser.

Fig. 12(b) shows an example of the PSD spectrum at 25 °C from two hybrid lasers biased at 150 mA. The red curve is the result from a laser with stronger feedback (higher coupling efficiency) and the blue curve is the result from a laser with weaker feedback (lower coupling efficiency). The Lorentzian linewidth is calculated from (3) where the white noise PSD level is used. From Fig. 12(b), laser linewidths $\Delta\nu$ of 1.1 MHz and 360 kHz are deduced respectively.

Fig. 13(a) shows a strong dependence of the measured laser linewidth $\Delta\nu$ versus ambient temperature and laser drive currents, for an assembly with low coupling loss (-1.5 dB) and strong optical feedback. As mentioned before, the SiN grating coupler has an estimated back-reflection strength of 4% (-14 dB). The effect of external feedback on the laser linewidth $\Delta\nu$ is a function of the feedback strength and phase [25], [26]. The periodic variation of $\Delta\nu$ over temperature for a given drive current, suggests that it is mostly influenced by the back-reflected signal coming from the SiN grating coupler, as the thermally-driven

TABLE I
DESCRIPTION OF INITIAL RELIABILITY TESTS

Method	Test conditions	Learning
Shear test	Force applied until LD peels off	Mechanical stability
Moisture Sensitivity Level (MSL1)	Bake for 24h at 125°C Soak at 85°C/85% RH for 168h 3 times reflow at 260°C	Underfill performance Laser operation

relative phase shift matches with the 1.2 mm-long roundtrip path in the SiN waveguide between the laser and the grating coupler (see Fig 2(a)). The relatively high intensity of the side modes seen in Fig. 13(b) is another consequence of this strong optical feedback. The laser linewidth $\Delta\nu$ ranges from 260 kHz to tens of MHz whereas the laser linewidth before bonding is in the range of 500 kHz to few MHz. As such, laser linewidth narrowing can be also achieved.

We then applied (4) to analyze the measured linewidth relationship with the feedback strength. Using (4), the estimated solitary laser linewidth is around 2.6 MHz and the effective feedback coefficient C is 0.56. These results show that the hybrid laser linewidth in the current assemblies is strongly affected by optical feedback from the grating coupler, and that the linewidth can be narrowed when the feedback phase is properly tuned.

D. Initial Reliability Tests

Flip-chip laser assemblies are prone to various potential degradation mechanisms, including laser displacement and stress, laser failure, μbump cracking/voiding, creep and diffusion of copper lines, degradation of the optical epoxy and more. Dedicated reliability tests need to be carried out to examine the failure rates for each degradation mechanism, using industry-standard tests such as accelerated ageing, thermal cycling, high temperature storage, electromigration, electro-static discharge test, vibration, etc.

As a first step toward comprehensive reliability testing, a first set of reliability tests was conducted, as listed in Table I.

First, we performed shear strength tests to evaluate the mechanical stability of the laser assemblies. We compared the shear force needed to peel off the laser without and with underfill. We tested 10 assemblies in each group, bonded using the same process conditions. Results are shown in Fig. 14. Looking at the mean values, the shear force needed to peel underfilled LDs is ~2.5 higher than for LDs without underfill (87.8 gf versus 36.5 gf, respectively). We compared this value with MIL-STD-883J shear strength standard for 350×300 μm die: the assembly withstands MILSPEC 1.25x of 81.4 gf [27].

Next, a humidity test (MSL1) was carried out, including exposure in a humidity chamber for 1 week, followed by 3 cycles of solder reflow conditions, mimicking a PCB attach process. Eight bonded and underfilled lasers were stressed under the conditions as described in Table I.

L-I curves of one assembly before and after stress are shown in Fig. 15. The fiber-coupled after-stress optical power variation relative to the pre-stress value was within 10% for all 8
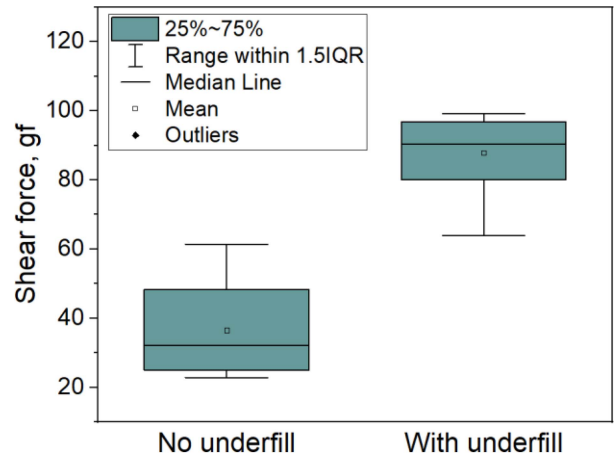

Fig. 14. Shear test results for assemblies with and without underfill.
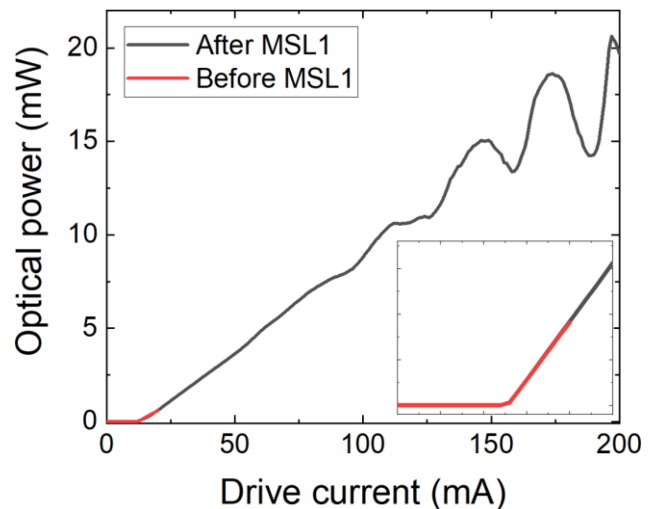

Fig. 15. L-I curves of laser assembly before and after MSL1 stress. Inset shows a magnification of threshold current area.

tested devices, which is within the measurement variability of the test setup. This suggests that the laser performance is not significantly affected by the applied stress conditions, e.g., the underfill did not degrade, or the LD was not displaced. Ongoing work includes extensive reliability tests as mentioned above.

IV. SUMMARY AND OUTLOOK

We demonstrated a wafer-scale InP laser diode flip-chip bonding process with passive alignment precision below 300 nm, driven by a visual fiducial recognition system in an advanced assembly tool, enabling a relatively high throughput of >100 devices per hour. Vertical alignment is controlled by limiting mechanical structures co-designed in both SiPho and laser diode. The electrical connection between the InP laser and the SiPho wafer is enabled by landing the laser Au contacts on standard CMOS Cu/Ni/Sn bumps followed by reflow, adding only ~1.1 Ohm extra series resistance. Optical coupling losses of -1.5 ± 0.5 dB are achieved in the C-band after optimizing the assembly and underfill process, and are close to the 1.1 dB

coupling loss predicted by 3D FDTD simulations. Leveraging the efficient heat sinking and low thermal resistance of the bonded lasers (26.6° K.mm/W), up to 40 mW of optical power coupled to the SiN waveguide at room temperature and a drive current of 200 mA. In-depth thermal modeling suggests that the main contribution to thermal resistance is lateral heat spreading within the laser diode.

The demonstrated laser assemblies suffered from strong unintentional optical feedback from non-optimized fiber grating couplers used for optical characterization, creating strong ripples in the measured L-I curves. A detailed study of the influence of these back-reflections on the Lorentzian linewidth and laser frequency noise was carried out. By thermo-optically tuning the feedback phase through temperature and drive current, we were able to decrease the Lorentzian linewith of a packaged DFB laser to 260 kHz, substantially lower than the Lorentzian linewidth of the lasers before bonding (500 kHz to few MHz).

Finally, a first set of reliability tests was carried out. Shear tests show a significant improvement in mechanical stability after underfill application, reaching shear strength of 828.6 gf/mm^2. Several laser assemblies have also passed an initial humidity and solder reflow test, providing a positive outlook for ongoing comprehensive reliability studies.

ACKNOWLEDGMENT

REFERENCES

[1] M. Rakowski et al., "Hybrid 14 nm FinFET - Silicon Photonics technology for low-power Tb/s/mm^2 optical I/O," in *Proc. IEEE Symp. VLSI Technol.*, 2018, pp. 221–222.

[2] Continuous-Wave Wavelength Division Multiplexing Multi-Source Agreement Consortium, "Technical specifications rev 1.0," Accessed: Jun. 4, 2021, [Online]. Available: http://cw-wdm.org/?wpdmdl=2092

[3] E. Canoglu et al., "Semiconductor lasers and optical amplifiers for LiDAR photonic integrated circuits," in *Proc. IEEE 27th Int. Semicond. Laser Conf.*, 2021, pp. 1–2.

[4] M. Theurer et al., "Flip-Chip integration of InP to SiN photonic integrated circuits," *IEEE J. Lightw. Technol.*, vol. 38, no. 9, pp. 2630–2636, May 2020.

[5] A. Hermans et al., "High-pulse-energy III-V-on-silicon-nitride mode-locked laser," *APL Photon.*, vol. 6, 2021, Art. no. 096102.

[6] Y. Hu et al., "III/V-on-Si MQW lasers by using a novel photonic integration method of regrowth on a bonding template," *Light: Sci. Appl.*, vol. 8, 2019, Art. no. 93.

[7] D. Colucci et al., "Unique design approach to realize an O-band laser monolithically integrated on 300 mm Si substrate by nano-ridge engineering," *Opt. Exp.*, vol. 30, pp. 13510–13521, 2022.

[8] S. Venkatesan et al., "A wafer scale hybrid integration platform for Co-packaged photonics using a CMOS based optical InterposerTM," in *Proc. IEEE Symp. VLSI Technol. Circuits*, 2022, pp. 381–382.

[9] I. Ghannam, B. Shen, F. Merget, and J. Witzens, "Silicon nitride external cavity laser with alignment tolerant multi-mode RSOA-to-PIC interface," *IEEE J. Sel. Topics Quantum Electron.*, vol. 28, no. 1, pp. 1–10, Jan./Feb. 2022.

[10] D. Vermeulen et al., "Reflectionless grating couplers for silicon-on-insulator photonic integrated circuits," *Opt. Exp.*, vol. 20, pp. 22278–22283, 2012.

[11] B. Buscaino, E. Chen, J. W. Stewart, T. Pham, and J. M. Kahn, "External vs. integrated light sources for intra-data center co-packaged optical interfaces," *IEEE J. Lightw. Technol.*, vol. 39, no. 7, pp. 1984–1996, Apr. 2021.

[12] M. N. Sysak et al., "Experimental and theoretical thermal analysis of a hybrid silicon evanescent laser," *Opt. Exp.*, vol. 15, no. 23, pp. 15041–15046, Nov. 2007.

[13] B. Song, L. Megalini, S. Dwivedi, S. Ristic, and J. Klamkin, "High-thermal performance 3D hybrid silicon lasers," *IEEE Photon. Technol. Lett.*, vol. 29, no. 14, pp. 1143–1146, Jul. 2017.

[14] B. Song, C. Stagarescu, S. Ristic, A. Behfar, and J. Klamkin, "3D integrated hybrid silicon laser," *Opt. Exp.*, vol. 24, no. 10, pp. 10435–10444, May 2016.

[15] R. Loi et al., "Thermal analysis of InP lasers transfer printed to silicon photonics substrates," *IEEE J. Lightw. Technol.*, vol. 36, no. 24, pp. 5935–5941, Dec. 2018.

[16] D. Shin et al., "Bulk-Si platform: Born for DRAM, upgraded with on-chip lasers, and transplanted to LiDAR," *J. Lightw. Technol.*, vol. 40, no. 10, pp. 3137–3148, May 2022.

[17] Hexagon AB, MSC Software Corporation, "Marc: Advanced nonlinear simulation solution," Accessed: Aug. 22, 2022. [Online]. Available: https://hexagon.com/products/marc

[18] D. Coenen et al., "Thermal characterization of hybrid, flip-chip InP-Si DFB lasers," *J. Lightw. Technol.*, to be published.

[19] P. J. Winzer, "High-spectral-efficiency optical modulation formats," *IEEE J. Lightw. Technol.*, vol. 30, no. 24, pp. 3824–3835, Dec. 2012.

[20] P. F. McManamon, "Review of ladar: A historic, yet emerging, sensor technology with rich phenomenology," *Opt. Eng.*, vol. 51, no. 6, Jun. 2012, Art. no. 060901.

[21] C. Henry, "Phase noise in semiconductor lasers," *IEEE J. Lightw. Technol.*, vol. 4, no. 3, pp. 298–311, Mar. 1986.

[22] L. Columbo, J. Bovington, S. R.-Garcia, D. F. Siriani, and M. Gioannini, "Efficient and optical feedback tolerant hybrid laser design for silicon photonics applications," *IEEE J. Sel. Topics Quantum Electron.*, vol. 26, no. 2, pp. 1–10, Mar./Apr. 2020.

[23] G. Morthier, "Feedback sensitivity of DBR-Type laser diodes," *IEEE Photon. J.*, vol. 13, no. 4, pp. 1–5, Aug. 2021.

[24] M. A. Tran, D. Huang, and J. E. Bowers, "Tutorial on narrow linewidth tunable semiconductor lasers using Si/III-V heterogeneous integration," *APL Photon.*, vol. 4, no. 11, Nov. 2019, Art. no. 111101.

[25] K. Petermann, "External optical feedback phenomena in semiconductor lasers," *IEEE J. Sel. Topics Quantum Electron.*, vol. 1, no. 2, pp. 480–489, Jun. 1995.

[26] N. Schunk and K. Petermann, "Numerical analysis of the feedback regimes for a single-mode semiconductor laser with external feedback," *IEEE J. Quantum Electron.*, vol. 24, no. 7, pp. 1242–1247, Jul. 1988.

[27] U.S. Department of Defense, MIL-STD-883J – Test method standard for microcircuits, Accessed: Sep. 16, 2019. [Online]. Available: https://landandmaritimeapps.dla.mil/Downloads/MilSpec/Docs/MIL-STD-883/std883.pdf

Aleksandrs Marinins received the B.Sc. and M.Eng. degrees from Riga Technical University, Riga, Latvia, in 2013, and the Ph.D. degree in integrated photonics from the KTH Royal Institute of Technology, Stockholm, Sweden, in 2017. He joined IMEC in 2018 and is currently working as silicon photonics laser packaging Engineer.

Sebastian Hänsch received the B.Sc. and M.Sc. degrees in physics from the University of Regensburg, Regensburg, Germany, in 2010 and 2014, respectively. He is currently an Advanced Application Engineer and Project Leader for ASMPT, the worldwide leading supplier of ultra-high-precision systems specializing in submicron placement accuracy ($\pm 0.2\mu$m@3 s) and an expert with focus on eutectic, laser- and uv-based bonding-processes.

Huseyin Sar received the M.S. and Ph.D. degrees in electrical engineering from the Eskisehir Technical University, Eskisehir, Turkey, in 2014 and 2019, respectively. In 2020, he was a Postdoctoral Research Associate with the Nanoscale Optic Lab, Missouri Science and Technology University, Rolla, MO, USA. Since 2021, he has been a Research and Development Engineer in IMEC, Belgium, working on silicon photonics with an emphasis on developing test routines for silicon photonics.

François Chancerel received the M.S. degree in nanotechnology engineering from the Institut National des Sciences Appliquées, Rennes, France, in 2013, and the joint Ph.D. degree in materials sciences engineering from the University of Sherbrooke, Sherbrooke, QC, Canada, and from Ecole Centrale de Lyon, Ecully, France, in 2018. He is currently an R&D Engineer at IMEC, working on bonding applications with an emphasis on semiconductors heterogeneous integration and layer transfer.

Negin Golshani received the B.S. degree in electrical engineering from the University of Tabriz, Tabriz, Iran, and the M.S. and Ph.D. degrees in microelectronics from the Delft University of Technology, Delft, The Netherlands, in 2009 and 2015, respectively. She is currently a Research and Development integration Engineer with IMEC, working on silicon photonics integration.

Hsiao-Lun Wang received the B.S. degree in engineering science and the M.S. degree in electrical engineering from National Taiwan University, Taipei, Taiwan, in 2010 and 2013, respectively. He received the Ph.D. degree from the University of Illinois Urbana–Champaign, IL, USA, in 2020. From 2015 to 2020, he worked as a Graduate Research Assistant under supervision of Prof. M. Feng and his research focus was high-speed oxide VCSELs development for short-reach optical links. He is currently a Postdoctoral Researcher affiliated with Ghent University and IMEC, Belgium. His research interests focus on semiconductor laser design and integration with silicon photonics.

Artemisia Tsiara received the M.Sc. degree in electrical, electronics and communications engineering from Aristotle University of Thessaloniki, Thessaloniki, Greece, in 2015, and the Ph.D. degree from Université Grenoble Alpes, Grenoble, France, in 2019. From 2015 to 2018, she was in CEA-Leti working on the reliability characterization of nanowire transistors for sub-10 nm nodes. Since 2018, she has been a Researcher on silicon photonics reliability with the reliability group of IMEC, Leuven, Belgium.

David Coenen (Student Member, IEEE) received the M.S. degree in aerospace engineering from KU Leuven, Leuven, Belgium, in 2018, and M.Sc. degree in electromechanical engineering from Ghent University, Ghent, Belgium, in 2020. He is currently working toward the Ph.D. degree at IMEC and KU Leuven, focusing on thermal management of optical transceivers.

Peter Verheyen received the degree in electrical engineering and the Ph.D. degree from Katholieke Universiteit Leuven, Leuven, Belgium, in 1996 and 2003, respectively. He was a Doctoral Researcher with the Interuniversity Microelectronics Center, Leuven, involved in advanced CMOS integration and MEMS integration. He is currently a member of the Silicon Photonics staff as a part of the 3D integration group, leading the Silicon Photonics Integration team.

Giovanni Capuz received the B.Sc. degree in electrical engineering at the Technological Institute of the Philippines, Manila, Philippines, in 1996. He earned 95 percentile rank in the National Licensure board examination for Registered Electrical Engineers. He worked in the industrial aspect of semiconductor advanced packaging Flip chip and BGA/SiP/MCM in different OSATs in Asia for 15 years. He is currently an R&D Project Leader in IMEC, Belgium, for 10 years, with past assignment on research about 3D/2.5D stacking and D2W assemblies. He is currently working on NPI projects for packaging ASICs through ICLink, the industrial arm of IMEC.

Yannick De Koninck received the master's degree in photonics engineering in 2009, and the Ph.D. degree in micro laser integration for silicon photonics, in 2015, both from Ghent University, Ghent, Belgium. From 2014 to 2018, he was a Senior Design Engineer at Luxtera, CA, USA, and from 2018 to 2021, he worked for IMEC exploring different laser integration approaches. In 2021, he joined NVIDIA and is now working on the next generation of silicon photonics transceiver technology.

Ozan Yilmaz received the B.Sc. degree in electrical engineering from Yeditepe University, Istanbul, Turkey, in 2001, and the M.Sc. degree from Boğaziçi University, Istanbul,Turkey, in 2004, and the second M.Sc. degree from the University of Central Florida, Orlando, FL, USA, in 2006. He received the Ph.D. degree from the University of North Carolina, Chapel Hill, NC, USA, in 2012. He is currently he is with Aeva Technologies, working on lasers for LiDAR applications.

Geert Morthier received the degree in electrical engineering and the Ph.D. degree from Ghent University, Ghent, Belgium, in 1987 and 1991, respectively. Since 1991, he has been a member of the permanent staff of IMEC. He was the Project Manager of the ACTS Project ACTUAL (1998–1999), dealing with the control of widely tunable laser diodes; the IST Project NEWTON (2001–2005) on new widely tunable lasers; the FP7 Project HISTORIC (2008–2011) on microdisk lasers. Since 2001, he has been apart-time Professor with Ghent University. He has authored or co-authored more than 200 papers in the field and holds several patents. He is also one of the two authors of the Handbook of Distributed Feedback Laser (Artech House, 1997). He has been on the TPC of several conferences (e.g., OFC and ECOC). His research interests include the modeling and characterization of optoelectronic components.

Filip Schleicher received the Ph.D. degree from the University of Strasbourg, Strasbourg, France, in 2012. His work was heavily fabrication oriented, with strong focus on mask design, thin film growth, lithography, etch and electrical characterization of final devices. After a cooperative Postdoctoral position shared between IPCMS,Strasbourg and IJL, Nancy, he joined the dry etch team at IMEC, in 2019. His research interests include N3 BEOL applications, lines/spaces, contact holes, and various 3D integration schemes.

Geraldine Jamieson received the M.Sc. degree in physical chemistry from the University of Natal, Pietermaritzburg, South Africa, in 1988, and a Higher Educational Teaching diploma, in 1989. She was a physical science Teacher with Wartburg and Montebello High School, Wartburg, South Africa (1989–1992), and a physical chemistry Lecturer with the University of Namibia, Windhoek, Namibia (1992–1996). She worked at an IMEC Packaging Spin-off company (CS2)(2000-2002), and then joined IMEC in 2002 as a Process Technologist. Her role evolved to a Process Development Engineer in the Etch team. She is currently a Senior Process Engineer in the Fab Etch team where she is involved in diverse projects across IMEC for etch development and process stabilization in both the 200 and 300 mm Fab.

Stuart Smyth received the B.Sc. (Hons) degree in physics from the University of Strathclyde, Glasgow, U.K., in 2019. He is currently a Device Engineer with Sivers Photonics, working on laser sources for silicon photonics applications.

Andrew McKee received the B.Eng. (Hons) degree in electronic engineering and the Ph.D. degree from the University of Glasgow, Glasgow, U.K., in 1996. He has extensive experience in all aspects of III-V optoelectronic device design and manufacture, gained with Agilent Technologies. He is Founder of Sivers Photonics, and currently the CTO, and is responsible for the technical roadmap of the company including developing new laser-device designs and process-integration technologies. His research interests focus on the area of Quantum Well Intermixing (QWI) of InGaAsP MQW structures for Photonic Integrated Circuits.

Yoojin Ban received the M.E. degree in electrical and electronics engineering from Yonsei University, Seoul, South Korea, in 2015, for her works on Si photonics modulator development. For six years after that she was responsible for the Si modulator devices and Si Photonics optical transceiver at IMEC. Since 2021, she has been Program Manager of the industry-affiliation R&D program on Optical I/O at IMEC, which targets the development of a scalable and industrially viable short-reach optical interconnect technology based on silicon photonics.

Marianna Pantouvaki (Member, IEEE) received the Ph.D. degree on long-distance optical communication systems from University College London, London, U.K. From 2006 to 2021, she was with IMEC, developing silicon photonics for optical interconnects. She is currently with Microsoft Research U.K., working on integrated photonics for cloud systems.

Douglas Charles La Tulipe received the B.Sc. degree in chemistry from the Western Connecticut State University, Danbury, CT, USA, in 1988. From 1984 to 2013, Douglas was with IBM Thomas J. Watson Research Center, Albany, NY, where he worked on 3D integration. From 2013 to 2020, he was with SUNY Poly, Albany, NY, USA. From 2020 to 2022, he worked at IMEC, Leuven, Belgium, as a 3DSIP path finding R&D Group Manager. He is currently with Draper Lab, Cambridge, MA, USA.

Joris Van Campenhout (Member, IEEE) received the M.S. degree in engineering physics in 2002, and the Ph.D. degree in electrical engineering in 2007, from Ghent University, Ghent, Belgium. He is currently Fellow Silicon Photonics with IMEC, Leuven, Belgium, and the Director of the industry-affiliation R&D program on Optical I/O, which seeks to substantially scale optical interconnects to bandwidth densities beyond 1Tbps/mm, while consuming less power than 1pJ/bit.